Surface profile and stress field evaluation using digital gradient sensing method

2016 Meas. Sci. Technol. 27 095203

(http://iopscience.iop.org/0957-0233/27/9/095203)

IOP Publishing Measurement Science and Technology
Meas. Sci. Technol. **27** (2016) 095203 (16pp) doi:10.1088/0957-0233/27/9/095203

Surface profile and stress field evaluation using digital gradient sensing method

C Miao[1], B M Sundaram[1], L Huang[2] and H V Tippur[1,3]

[1] Department of Mechanical Engineering, Auburn University, Auburn, AL 36849, USA
[2] Brookhaven National Laboratories, Upton, NY 11973, USA

E-mail: tippuhv@auburn.edu

Received 15 April 2016, revised 22 June 2016
Accepted for publication 5 July 2016
Published 9 August 2016

Abstract

Shape and surface topography evaluation from measured orthogonal slope/gradient data is of considerable engineering significance since many full-field optical sensors and interferometers readily output such a data accurately. This has applications ranging from metrology of optical and electronic elements (lenses, silicon wafers, thin film coatings), surface profile estimation, wave front and shape reconstruction, to name a few. In this context, a new methodology for surface profile and stress field determination based on a recently introduced non-contact, full-field optical method called digital gradient sensing (DGS) capable of measuring small angular deflections of light rays coupled with a robust finite-difference-based least-squares integration (HFLI) scheme in the Southwell configuration is advanced here. The method is demonstrated by evaluating (a) surface profiles of mechanically warped silicon wafers and (b) stress gradients near growing cracks in planar phase objects.

Keywords: optical metrology, speckle correlation, surface slopes, stress gradients, surface topography, stress evaluation

(Some figures may appear in colour only in the online journal)

1. Introduction

There is a demand for an accurate, non-contact evaluation of surface topography of objects. Some optical sensors such as the Shack–Hartmann wave-front sensor [1], the lateral shearing interferometers [2], and the pyramid sensor [3] have all been used for this purpose. The current literature indicates that it is more efficient for these sensors to just measure the surface gradients instead of measuring the values of absolute height due to channel capacity limitations [4]. Integration algorithms are applied then to convert the measured gradients into topographic information. It can be concluded that a highly accurate, non-contact method for measuring surface gradients in combination with an accurate integration method are among the key factors to satisfactorily reconstruct surface topography.

As already noted, several optical metrology techniques for measuring surface gradients currently exist. Based on the type of illumination used, they can be divided into two categories, coherent (interferometric) and incoherent (moiré) methods [5–9]. In these, measurements are typically in the form of optical fringes and are analog in nature. Further, orthogonal gradients are generally evaluated by performing multiple or successive experiments (e.g. coherent gradient sensing or CGS method [7, 8]) which may require altering the setup. Also, the optical phase evaluation using phase shifting methods is often needed to determine gradients in the digital form. In recent years, however, digital image correlation (DIC) methods have become rather popular for measuring deformations, two or all three orthogonal displacements in the whole field, as they offer many advantages besides directly providing the required information in the digital form [10–13]. By taking advantage of this, a new full-field optical method called digital gradient sensing (DGS) method has been proposed recently for measuring two orthogonal small angular deflections of light rays caused by stresses in planar solids [14, 15]. Subsequently, the method has also been extended to study optically reflective objects as well [16]. The simplicity of experimental setup, its accuracy and robustness make DGS attractive for measuring two orthogonal surface slopes and

[3] McWane Endowed Chair Professor.

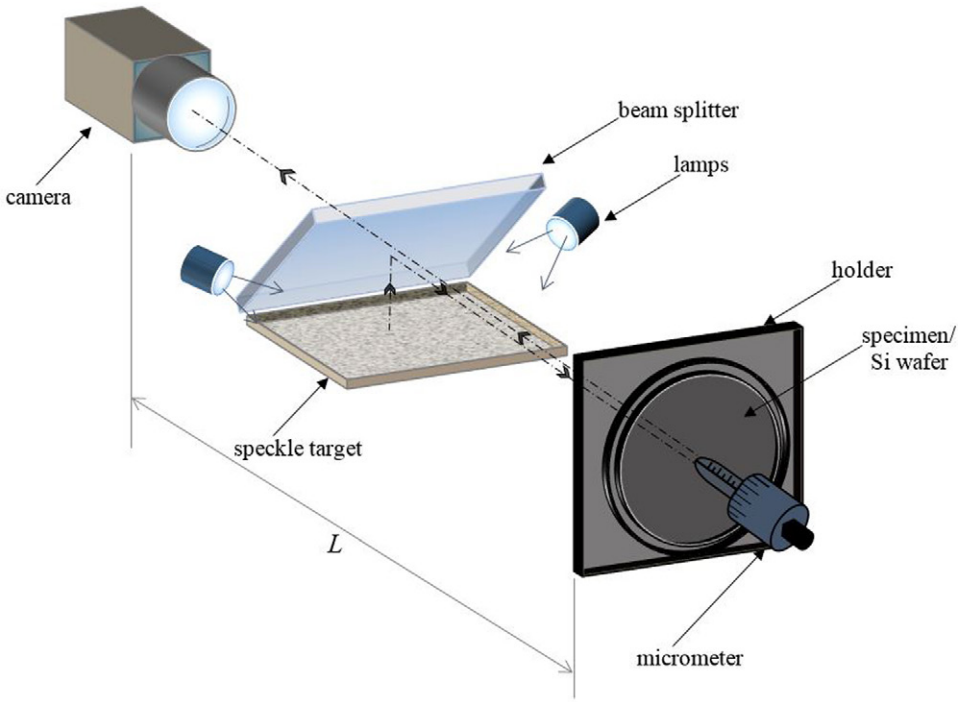

Figure 1. Schematic of r-DGS experimental setup.

stress gradients in the whole field. Subsequent quantification of surface profile or stresses from these measurements via 2D integration of measured data is valuable in many engineering applications.

There are several 2D integration methods reported in the literature. Broadly, they can be divided into two types: path dependent integration methods [17–19] and path independent integration methods [4, 20–24]. Path dependent integration methods such as trapezoidal rule or Simpson's rule calculate the local height increments by directly integrating the function. These methods are easy to implement due to the simplicity and efficiency in computing. However, the accuracy of results from these methods depends heavily on integration paths. Noise in measured data can propagate and accumulate along the integration path. Such errors can be mitigated in path independent integration methods because gradient data have global influence on the solution procedures and errors get uniformly dispersed over the whole surface [25].

Methods based on Fourier transforms [20] are a family of path independent integration methods which are fast and accurate. However, these methods cannot deal with irregular surface shapes which make it not very practical. Another family of path independent integration methods, which can also be fast and highly accurate, is least-squares based integration methods [21–24]. Hudgin [21] proposed a least-squares recursive algorithm for wave-front reconstruction from phase difference and studied the propagation of noise. Southwell [22] proposed a more detailed least-squares integration algorithm for wave-front reconstruction based on a rectangular grid configuration. Huang *et al* [23] pointed out the assumption of biquadratic functions in Southwell grid configuration limited the algorithm. They proposed an optimized algorithm by implementing iterative compensations. Li *et al* [24] pointed out that Huang's

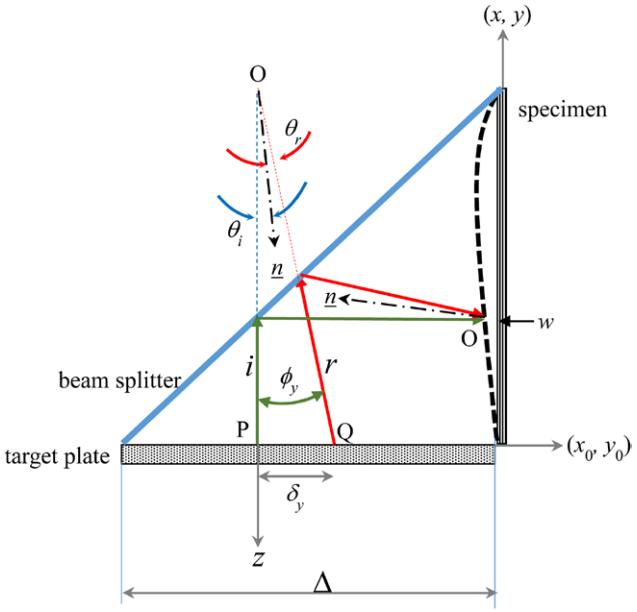

Figure 2. Schematic explaining the working principle of r-DGS.

algorithm was rather time consuming although the accuracy of reconstruction was significantly improved, and hence proposed a more accurate and less time intense approach. Ettl *et al* [4] proposed another kind of integration method by using radial basis functions which showed robustness and high accuracy. However, compared with Li's method, it was found time consuming, especially when the dataset is incomplete. Huang *et al* [26] compared three families of 2D integration methods: (a) the Finite-difference-based least-squares integration methods, (b) the transform-based integration methods and (c) the Radial basis function based integration methods. Their performance, advantages and weaknesses are discussed in details

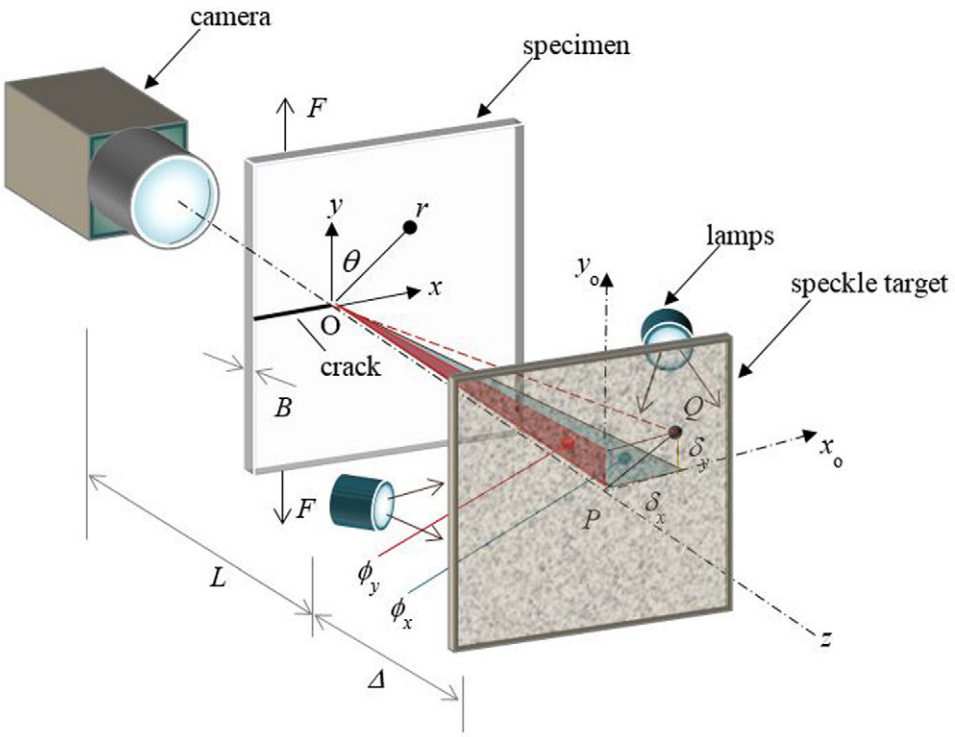

Figure 3. The schematic of the experimental setup for t-DGS technique to determine planar stress gradients in phase objects.

for specific cases. Accordingly, Li *et al*'s algorithm [24] is selected in the current work.

In the following, the experimental details and working principle of both reflection-mode DGS (r-DGS) and transmission-mode DGS (t-DGS) are briefly presented. Next, the algorithm of the 2D integration method is explained along with its verification using an idealized function. Then, the feasibility of the 2D integration method in conjunction with r-DGS is discussed in detail using a Si wafer subjected to central and eccentric out-of-plane loading. This is followed by the demonstration of extracting stress fields from measured stress gradients from t-DGS. Finally, the major results of this study are summarized.

2. Experimental setup and working principle

2.1. Reflection-mode digital gradient sensing (r-DGS)

A schematic of the experimental setup for r-DGS used to measure surface slopes is shown in figure 1. A digital camera, a reflective planar specimen, a micrometer, a beam splitter and a target plate are included in the figure. The target plate is decorated with random speckles using alternate mists of black and white paints. The beam splitter is placed between the specimen and target plate at an angle of 45° to the optical axis of the setup for the camera to photograph the speckles on the target via the specimen surface. The target plate is illuminated by a pair of cool LED lamps emitting white light.

For simplicity, the angular deflections of light rays only in the y-z plane are shown in figure 2. Initially, a point P on the target plate is recorded by the camera through a point O when the specimen is in its undeformed or reference state. When the specimen suffers out-of-plane deformation, a neighboring point Q on the target gets recorded by the camera through O. OP makes an angle ϕ_y with OQ and $\phi_y = \theta_i + \theta_r$ where θ_i and $\theta_r(=\theta_i)$ are incident and reflected angles relative to the normal to the specimen. The two orthogonal surface slopes can be expressed as $\frac{\partial w}{\partial y:x} = \frac{1}{2}\tan(\phi_{y:x})$. The local displacements $\delta_{y:x}$ can be measured by correlating the undeformed image of the specimen with respect to the deformed image. Finally, the two orthogonal surface slopes can be determined using [16]:

$$\frac{\partial w}{\partial y:x} = \frac{1}{2}\tan(\phi_{y:x}) \approx \frac{1}{2}(\phi_{y:x}) \approx \frac{1}{2}\left(\frac{\delta_{y:x}}{\Delta}\right) \qquad (1)$$

where Δ is the distance between the specimen and target plate and small angle approximation is evoked.

The experimental parameters including Δ, speckle characteristics on target plate, sub-image size used for image correlation control the accuracy of the method and the details can be found in [27]. Further, it should be noted here that the camera is focused on the target plane and the coordinates of the specimen plane are used in the analysis subsequently. Therefore, based on the pin-hole camera approximation, a mapping function is used to transfer the information to the specimen plane as, $(x:y) = \frac{L}{L+\Delta}(x_0:y_0)$ where $(x:y)$ and $(x_0:y_0)$ denote the coordinates of the specimen and target planes, respectively, and L is the distance between the specimen and camera [14].

2.2. Transmission-mode digital gradient sensing (t-DGS)

A schematic of the experimental setup for t-DGS method is shown in figure 3. Unlike r-DGS, in t-DGS a random speckle pattern on target plate is recorded through a transparent

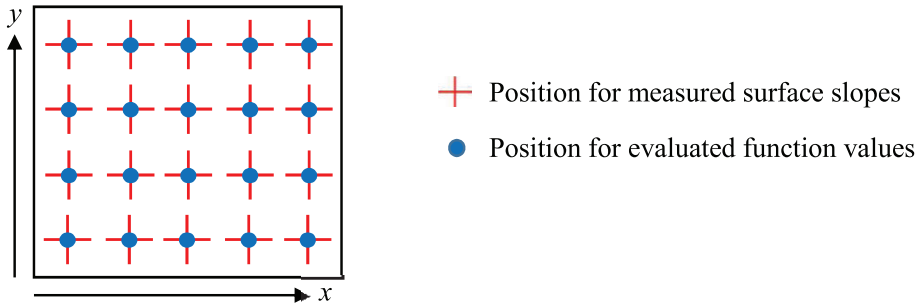

Figure 4. Southwell grid configuration.

specimen. White light is used here to illuminate the target. As in r-DGS, an undeformed or reference image is recorded first. That is, point P on the target plate which corresponds to point O on the specimen plane is recorded. The refractive index and thickness of the specimen change after imposing a load on the specimen. As a result, light rays from the initial path, which is referred to as the elasto-optical effect. In the deformed state of the specimen, an image is recorded. That is, a neighboring point of P, namely Q on the target plate is recorded through O on the specimen plane. The local displacements $\delta_{y:x}$ are measured by correlating the undeformed image with the deformed image of the specimen. The angular deflections of light rays $\phi_{y:x}$, which are related to in-plane stress gradients, can be expressed as [15]:

$$\phi_{x:y} \approx \frac{\delta_{x:y}}{\Delta} = C_\sigma B \frac{\partial(\sigma_{xx} + \sigma_{yy})}{\partial(x:y)} \tag{2}$$

where C_σ is the elasto-optical constant of the specimen material, B is its initial thickness, Δ is the distance between the specimen and target plate, and $\sigma_{xx} + \sigma_{yy}$ is the sum of two in-plane normal stresses. Again, the pin-hole camera mapping function is used here to transfer coordinates of the target to the specimen.

3. The 2D integration method

The above two full-field optical methods, r-DGS and t-DGS, provide two orthogonal surface slopes and stress gradients in the region of interest as a rectangular array of data. Traditionally, surface topography and stresses in addition to or in place of surface slopes and stress gradients from such measurements are quite useful in engineering applications. Hence, reconstructing the same from DGS is valuable.

In the field of surface reconstruction from slope data, 2D integration based on finite-difference is widely used to compute topographic values from gradient data by least-squares procedures. Southwell proposed a traditional finite-difference-based least-squares integration (TFLI) algorithm for a grid configuration, as shown in figure 4, requiring the measured surface slopes and the evaluated topographic values are at the same spatial position [22, 26]. The relation between the slopes and the evaluated function values in a $M \times N$ matrix in this approach can be expressed as [26]:

$$\begin{cases} \dfrac{f_{m,n+1} - f_{m,n}}{x_{m,n+1} - x_{m,n}} = \dfrac{s^x_{m,n+1} + s^x_{m,n}}{2}, & m = 1, 2, \ldots, M, \\ & n = 1, 2, \ldots, N-1. \\ \dfrac{f_{m+1,n} - f_{m,n}}{y_{m+1,n} - y_{m,n}} = \dfrac{s^y_{m+1,n} + s^y_{m,n}}{2}, & m = 1, 2, \ldots, M-1, \\ & n = 1, 2, \ldots, N. \end{cases} \tag{3}$$

where x, y are the local coordinates, s denotes the local surface slopes, f is the value of the function at (x, y). Equation (3) can be converted to a matrix form,

$$\boldsymbol{DF} = \boldsymbol{G} \tag{4}$$

where

$$\boldsymbol{D} = \begin{bmatrix} D^x \\ D^y \end{bmatrix} = \left[\begin{array}{ccccccccc} -1 & 0 & \cdots & 0 & 1 & 0 & \cdots & \cdots & 0 \\ 0 & -1 & 0 & \cdots & 0 & 1 & 0 & \cdots & 0 \\ \vdots & \vdots & \vdots & \vdots & \vdots & \vdots & \vdots & \vdots & \vdots \\ 0 & \cdots & \cdots & 0 & -1 & 0 & \cdots & 0 & 1 \\ \hdashline -1 & 1 & 0 & \cdots & \cdots & \cdots & \cdots & \cdots & 0 \\ 0 & -1 & 1 & 0 & \cdots & \cdots & \cdots & \cdots & 0 \\ \vdots & \vdots & \vdots & \vdots & \vdots & \vdots & \vdots & \vdots & \vdots \\ 0 & \cdots & \cdots & \cdots & \cdots & \cdots & 0 & -1 & 1 \end{array}\right]_{[(M-1)N+M(N-1)]\times MN} \tag{5}$$

$$\boldsymbol{F} = \begin{bmatrix} f_{1,1} \\ f_{2,1} \\ \vdots \\ f_{M,N} \end{bmatrix}_{MN\times 1} \tag{6}$$

$$\boldsymbol{G} = \begin{bmatrix} G^x \\ G^y \end{bmatrix} = \frac{1}{2}\left[\begin{array}{c} (s^x_{1,2} + s^x_{1,1})(x_{1,2} - x_{1,1}) \\ (s^x_{2,2} + s^x_{2,1})(x_{2,2} - x_{2,1}) \\ \vdots \\ (s^x_{M,N} + s^x_{M,N-1})(x_{M,N} - x_{M,N-1}) \\ \hdashline (s^y_{2,1} + s^y_{1,1})(y_{2,1} - y_{1,1}) \\ (s^y_{3,1} + s^y_{2,1})(y_{3,1} - y_{2,1}) \\ \vdots \\ (s^y_{M,N} + s^y_{M-1,N})(y_{M,N} - y_{M-1,N}) \end{array}\right]_{[(M-1)N+M(N-1)]\times 1} \tag{7}$$

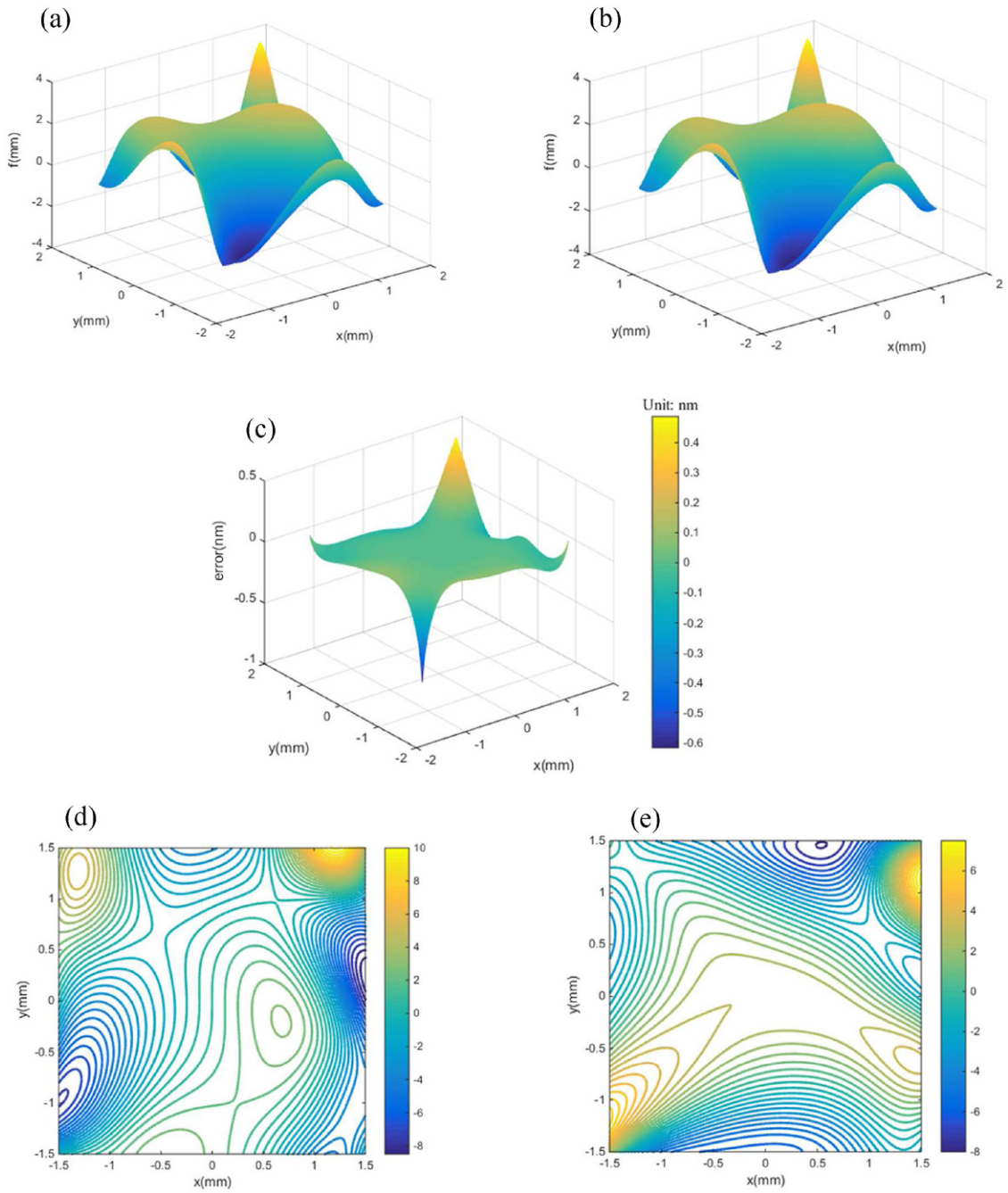

Figure 5. Verification of HFLI method. (a) Original function, (b) reconstructed function, (c) reconstruction errors, (d) contours of derivatives of the function in the *x*-direction, (e) contours of derivatives of the function in the *y*-direction.

Equation (4) can be solved to get $\boldsymbol{F}$as,

$$\boldsymbol{F} = (\boldsymbol{D}^T\boldsymbol{D})^{-1}\boldsymbol{D}^T\boldsymbol{G} \tag{8}$$

where $\boldsymbol{D}^T$ denotes the transpose of $\boldsymbol{D}$.

The TFLI method is widely used for its simplicity and reliability. However, in equation (3) the left-hand side is approximately equal to the right-hand side. Using Taylor's theorem, it can be shown that this method has an error of $O(h^3)$ where h is the interval between two neighboring grid points [24]. In recent years, further research in this area has been reported specifically to improve the accuracy of the method. Huang *et al* [23] proposed iterative finite-difference-based least-squares integration (IFLI) method. They applied iterative compensations to enhance TFLI method. However, IFLI method is much more computationally time consuming although the accuracy of reconstruction is higher. Li *et al* [24] proposed a more accurate and less time consuming approach, the higher-order finite-difference-based least-squares integration

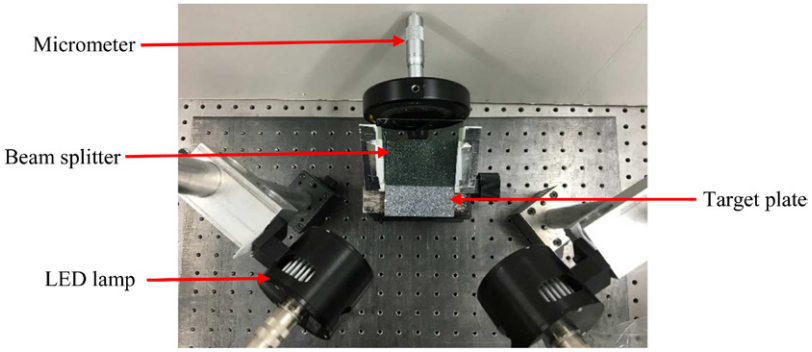

Figure 6. The experimental setup used to study out-of-plane deformation of a silicon wafer.

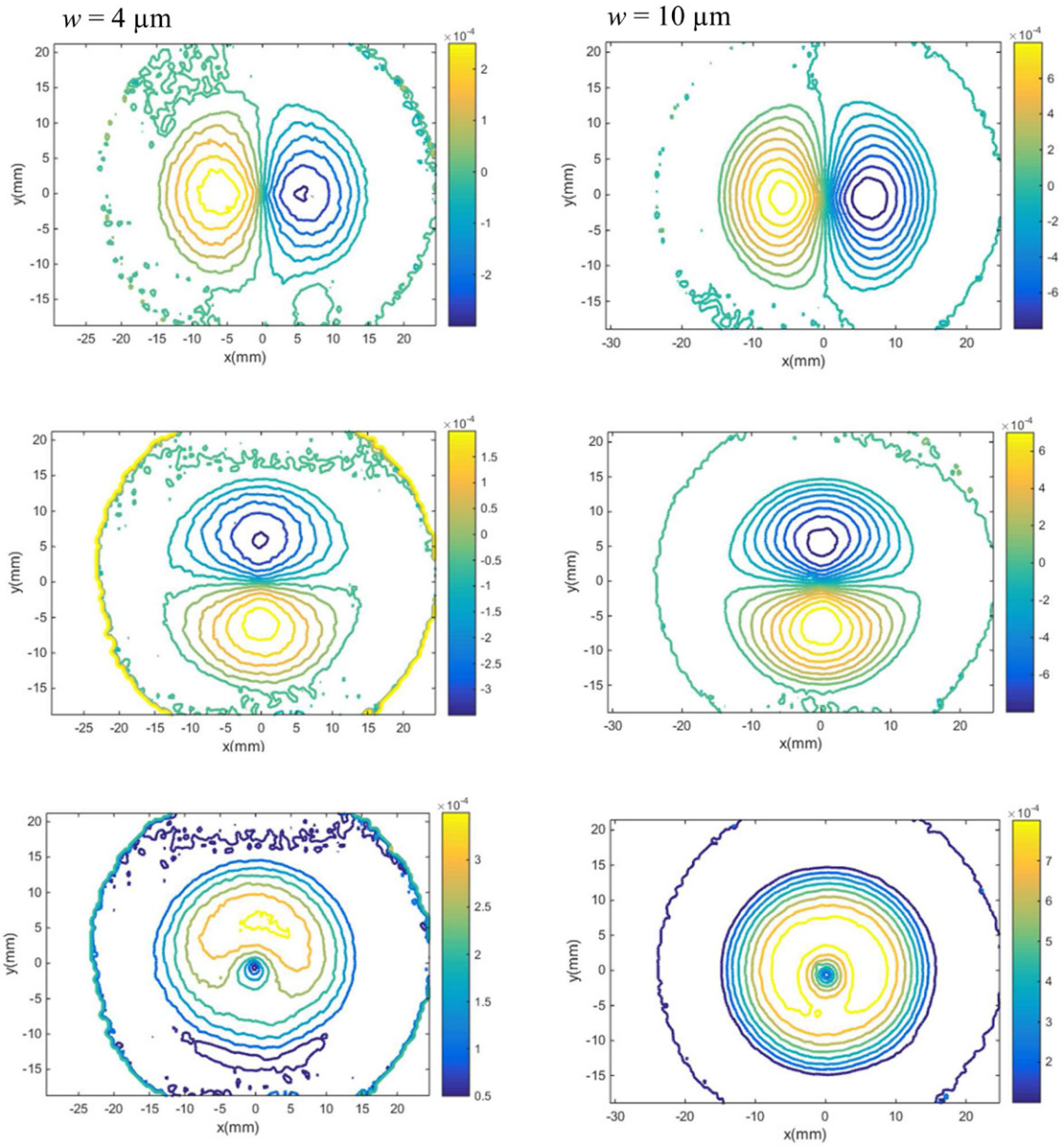

Figure 7. Results from r-DGS for a clamped silicon wafer (30 mm dia., 360 μm thick) subjected to central deflection of 4 μm (left column) and 10 μm (right column). Row 1: contours of $w_{,x}$; Row 2: contours of $w_{,y}$; Row 3: contours of $w_{,r}$. Note: (0, 0) is made to coincide with the loading point. Contour increments $= 0.5 \times 10^{-4}$ rad and 1×10^{-4} rad, respectively.

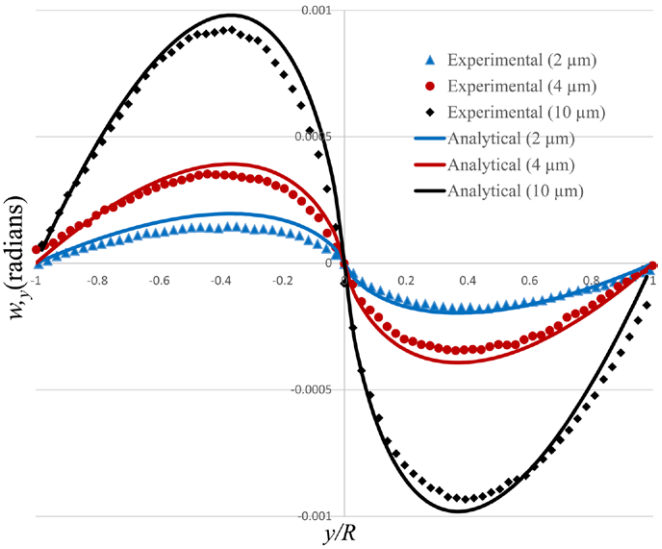

Figure 8. Comparison of analytical data and experimental data of $\frac{\partial w}{\partial y}$ along the y-axis corresponding to three different imposed out-of-plane deflections.

(HFLI) method. It applies Taylor's theorem and considers two additional adjacent slopes during iteration resulting in an algorithmic error of $O(h^5)$. In this method, the $\boldsymbol{G}$ matrix is expressed as[4]:

$$\boldsymbol{G} = \begin{bmatrix} G^x \\ G^y \end{bmatrix} \tag{9}$$

$$G^x = \frac{1}{24}\begin{bmatrix} 12(s^x_{1,2}+s^x_{1,1})(x_{1,2}-x_{1,1}) \\ 12(s^x_{2,2}+s^x_{2,1})(x_{2,2}-x_{2,1}) \\ \vdots \\ 12(s^x_{M,2}+s^x_{M,1})(x_{M,2}-x_{M,1}) \\ (-s^x_{1,4}+13s^x_{1,3}+13s^x_{1,2}-s^x_{1,1})(x_{1,3}-x_{1,2}) \\ (-s^x_{2,4}+13s^x_{2,3}+13s^x_{2,2}-s^x_{2,1})(x_{2,3}-x_{2,2}) \\ \vdots \\ (-s^x_{M,4}+13s^x_{M,3}+13s^x_{M,2}-s^x_{M,1})(x_{M,3}-x_{M,2}) \\ (-s^x_{1,5}+13s^x_{1,4}+13s^x_{1,3}-s^x_{1,2})(x_{1,4}-x_{1,3}) \\ \vdots \\ (-s^x_{M,5}+13s^x_{M,4}+13s^x_{M,3}-s^x_{M,2})(x_{M,4}-x_{M,3}) \\ \vdots \\ (-s^x_{M,N}+13s^x_{M,N-1}+13s^x_{M,N-2}-s^x_{M,N-3}) \\ (x_{M,N-1}-x_{M,N-2}) \\ 12(s^x_{1,N}+s^x_{1,N-1})(x_{1,N}-x_{1,N-1}) \\ 12(s^x_{2,N}+s^x_{2,N-1})(x_{2,N}-x_{2,N-1}) \\ \vdots \\ 12(s^x_{M,N}+s^x_{M,N-1})(x_{M,N}-x_{M,N-1}) \end{bmatrix}_{[(M-1)N]\times 1} \tag{10}$$

[4] A correction to the expression reported in [26] has been incorporated in these expressions.

$$G^y = \frac{1}{24}\begin{bmatrix} 12(s^y_{2,1}+s^y_{1,1})(y_{2,1}-y_{1,1}) \\ (-s^y_{4,1}+13s^y_{3,1}+13s^y_{2,1}-s^y_{1,1})(y_{3,1}-y_{2,1}) \\ (-s^y_{5,1}+13s^y_{4,1}+13s^y_{3,1}-s^y_{2,1})(y_{4,1}-y_{3,1}) \\ \vdots \\ (-s^y_{M-1,1}+13s^y_{M-2,1}+13s^y_{M-3,1}-s^y_{M-2,1}) \\ (y_{M-2,1}-y_{M-3,1}) \\ 12(s^y_{M,1}+s^y_{M-1,1})(y_{M,1}-y_{M-1,1}) \\ 12(s^y_{2,2}+s^y_{1,2})(y_{2,2}-y_{1,2}) \\ (-s^y_{4,2}+13s^y_{3,2}+13s^y_{2,2}-s^y_{1,2})(y_{3,2}-y_{2,2}) \\ \vdots \\ (-s^y_{M-1,2}+13s^y_{M-2,2}+13s^y_{M-3,2}-s^y_{M-2,2}) \\ (y_{M-2,2}-y_{M-3,2}) \\ 12(s^y_{M,2}+s^y_{M-1,2})(y_{M,2}-y_{M-1,2}) \\ 12(s^y_{2,3}+s^y_{1,3})(y_{2,3}-y_{1,3}) \\ (-s^y_{4,3}+13s^y_{3,3}+13s^y_{2,3}-s^y_{1,3})(y_{3,3}-y_{2,3}) \\ \vdots \\ 12(s^y_{M,N}+s^y_{M-1,N})(y_{M,N}-y_{M-1,N}) \end{bmatrix}_{[M(N-1)]\times 1} \tag{11}$$

3.1. Algorithm verification

To verify the accuracy of HFLI method independently, a function $f(x, y)$ was defined as follows:

$$f(x,y) = (x+y)\cos(x^2-y^2) + 2\sin(x^2+y)\cos(xy+y) \tag{12}$$

The chosen range for x and y coordinates for this demonstration were from -1.5 to 1.5 mm with an interval of 0.01 mm, resulting in a 300×300 data grid. As evident from figure 5(a) the function includes significant complexities in its features. The corresponding slope contours in the x- and y-directions are shown in figures 5(d) and (e), respectively. After removing the piston errors [28], the reconstructed function using HFLI algorithm is shown in figure 5(b). The integration errors shown in figure 5(c) indicate the high accuracy of HFLI method. The integration errors on the edges are somewhat higher because of the lack of two adjacent slopes on the edges as evident from equations (10) and (11). The mean values of errors in the region away from the edges are essentially zero or negligible.

4. Wafer subjected to central loading

The feasibility of HFLI method used in conjunction with r-DGS to obtain mechanically induced out-of-plane deformation maps for a deformed thin silicon wafer subjected to central loading was considered next. A single-face polished 360 μm thick silicon wafer of dimeter 50.8 mm was used in the experiment. The unpolished face was bonded to a thick steel washer with a circular aperture of 30 mm using a slow curing epoxy in order to simulate a thin circular plate with a circular clamped boundary. Another steel plate fitted with a micrometer at its center was positioned directly behind the silicon wafer. These two steel plates were secured in

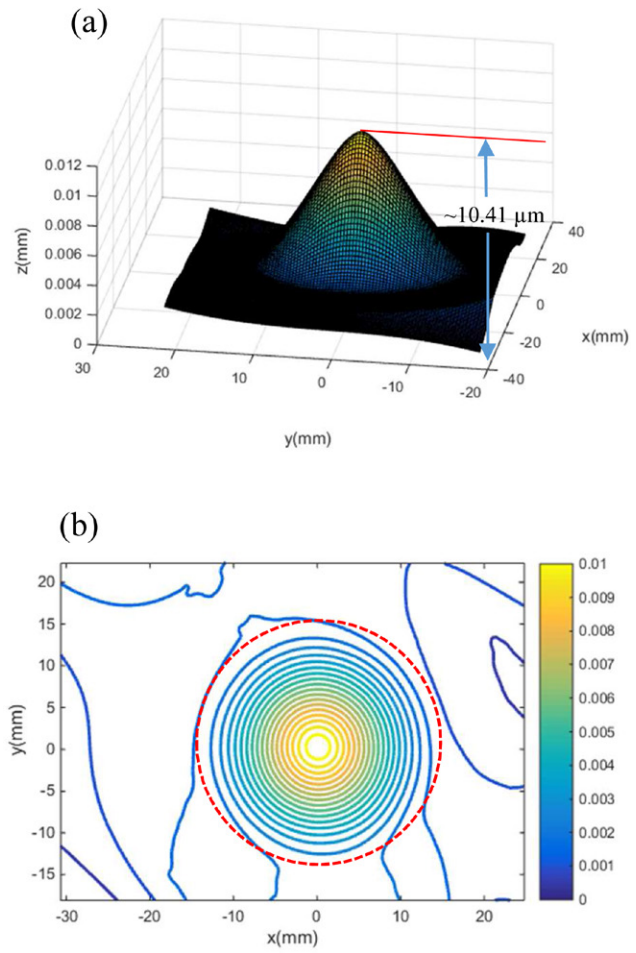

Figure 9. Surface topography calculated via 2D integration using surface slope data and HFLI method: (a) 3D surface representation of reconstructed surface, (b) out-of-plane displacement (w) contours (0.5 μm increments). Note: (0, 0) is made to coincide with the loading point; red circle indicates the edge of the circular aperture of the steel washer.

a cylindrical lens holder. A target plate, decorated with random black and white speckles, was placed horizontally at 90° to the silicon wafer. The target was illuminated by two cool LED lamps to avoid air currents. A beam splitter was placed at 45° to both the silicon wafer and the target plate. It was also at 45° to the optical axis of the camera (see figure 6). The distance (Δ) between the silicon wafer surface and the target plate along the optical axis was 62 mm.

A Nikon D100 digital SLR camera was focused on the target via the polished face of the silicon wafer. The camera was fitted with a 70–300 mm macro lens and an adjustable bellows. A small aperture ($F^{\#} = 22$) was selected for recording the speckles with a good focus. The distance between the silicon wafer and the end of lens (L) was 1403 mm. When the silicon wafer was under no load, an 8-bit reference image was recorded with a resolution of 1504 × 1000 pixels (1 pixel = 43.9 μm). Then, known central out-of-plane displacements, w, were imposed on the silicon wafer using the micrometer tip and speckle images corresponding to the deformed states of the wafer were recorded. By correlating each of these speckle images with the reference image, the local displacements $\delta_{y:x}$ in the region of interest were measured. During correlation (using ARAMIS image analysis software), the images were sub-divided into 20 × 20 pixels with 10 pixel overlap in the x- and y-directions, resulting in 97 × 133 matrix of data points in the field.

Two sets of orthogonal surface slope contours, $\frac{\partial w}{\partial x}$ and $\frac{\partial w}{\partial y}$ measured from r-DGS are shown in figure 7 for two imposed central deflections, 4 ± 1 μm and 10 ± 1 μm. For completeness, contours of $\frac{\partial w}{\partial r}\left(=\sqrt{\left(\frac{\partial w}{\partial x}\right)^2+\left(\frac{\partial w}{\partial y}\right)^2}\right)$ are also shown, where r is the radial distance from the center of the wafer. The contours are plotted with increments of 50 and 100 microradians in the two cases, respectively. It can be observed that the magnitude of contours of $\frac{\partial w}{\partial x}$ and $\frac{\partial w}{\partial y}$ are symmetric about $x = 0$ and $y = 0$ with a high concentration of contours near the loading point. The contours of $\frac{\partial w}{\partial r}$ show circular symmetry, again with a higher concentration of contours around the loading point. As expected, slopes are zero along the circular edge (and beyond) of the Si wafer in the glued portion and near the loading point with a gradual transition in the intermediate region.

The measurements from r-DGS are compared directly with the closed-form solutions for an elastic thin circular plate with a clamped boundary subjected to a centrally applied deflection using,

$$\frac{\partial w}{\partial y} = \frac{4yw}{R^2}\log\left(\frac{\sqrt{x^2+y^2}}{R}\right) \tag{13}$$

where w is the out-of-plane deformation and R is the radius of the circular plate.

The comparisons shown in figure 8 are made between experimental and analytical data sets along the y-axis for different magnitudes of out-of-plane deformations. The least count of the micrometer used being 2 μm, results from $w = 2$ μm is also added to this comparison. It can be readily observed that there is a good agreement between the two data sets with percentage error decreasing as imposed deflection is increased.

The reconstructed 3D surface computed using integration of surface slope data and HFLI computations is plotted in figure 9(a) for the 10 μm deflection case. Figure 9(b) shows the corresponding contours of out-of-plane displacements (w) at 0.5 μm increments. The circular contours in figure 9(b) demonstrates that the shape of the reconstructed figure matches well with the reality of the experiment both qualitatively and quantitatively. (Note that for all the plots in figures 7 and 9, the origin is made to coincide with the loading point.) The peak value of the height of the reconstructed 3D surface is 10.41 μm with an acceptable error of 4.1%. (The reconstruction for the smaller imposed deflection of 4 μm, not shown here for brevity, led to a peak value of 4.81 μm, a deviation of 20.2%. Given the uncertainty of the imposed deflection of ±1 μm, the reconstructed peak value is deemed reasonable despite a higher error.) The errors are

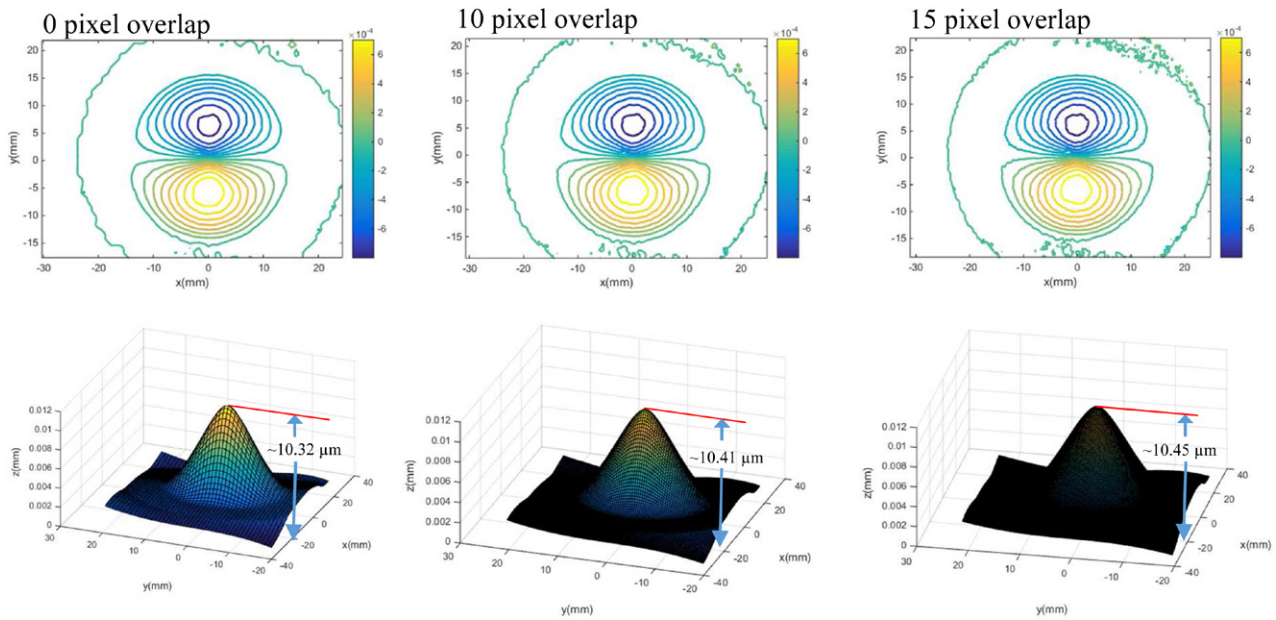

Figure 10. Contours of $w_{,y}$ for 20 × 20 pixel sub-images with three different overlap and the corresponding reconstructed figures.

attributed to a combined effect of (a) micrometer backlash and human errors while imposing the out-of-plane displacement, (b) the non-uniformity and finite compliance of the epoxy adhesive used to 'clamp' the Si wafer to the steel plate, (c) errors due to DGS measurements as well as integration errors in the HFLI method. Although it is beneficial to isolate each of these effects, it is difficult to do so practically. It should also be mentioned that the reconstructed surface along the glued boundary of the wafer shows non-zero deflection (approximately 1 μm instead of zero). This is attributed to a combination of reconstruction errors as well as compliance of the epoxy glue layer alluded to earlier.

The accuracy of HFLI method relies on the interval between two neighboring grid points. And, this interval in turn depends on the choice of sub-image size and pixel overlap used during correlation of the reference and deformed images while implementing r-DGS. Further, the overlap was selected for achieving correlation at all points in the region of interest with minimum noise in the plotted data. Therefore, the trade-offs if any due to different interval choices on HFLI outcome was examined. Figure 10 shows the measured contours of $\frac{\partial w}{\partial y}$ for 20 × 20 pixels sub-images with three different overlaps of 0, 10, 15 pixels and the corresponding reconstructed surfaces. Higher number of overlapping pixels resulted in the interval (h) between two neighboring grid points getting smaller. In figure 10, it can be observed that the slope contours are generally in good agreement with each other with minor differences between the slope contours near the wafer boundary where the slopes are expected to be zero. However, the interval (h) for 0 pixel overlap and 15 pixel overlap cases are different by a factor of 2 and 0.5 relative to the 10 pixel overlap case. The reconstructed surfaces for each of these cases are shown in figure 10. (Note that the plots appear darker as the grid density increases.) The difference of the peak values of out-of-plane displacement for the three cases relative to the imposed value range between 3.2% and 4.5% suggesting the robustness of the reconstruction. The height of the reconstructed surface for the zero pixel overlap case is the closest to 10 μm, however, it is less accurate due to the larger interval between neighboring grid points. As a result, 10 pixel overlap was judged appropriate for subsequent analyses.

5. Wafer subjected to eccentric loading

The measurement of slopes and reconstruction of out-of-plane deformations of a silicon wafer subjected to eccentric loading was attempted next. In this experiment, again out-of-plane displacements, $w = 4 \pm 1$ μm and 10 ± 1 μm, were imposed on the silicon wafer eccentrically at a distance of 5 mm away from the center of the wafer along the y-axis. Otherwise, the optical setup in this experiment was the same one used in the previous experiment. A 20 × 20 sub-image size with 10 pixel overlap was also used here to correlate the images in the deformed and undeformed states to get displacements $\delta_{y:x}$.

The two orthogonal surface slope contours, $\frac{\partial w}{\partial x}$ and $\frac{\partial w}{\partial y}$ for each of these imposed displacements are shown in figure 11. The contours of $\frac{\partial w}{\partial r}$ are also provided. As in the central loading case, all the contours are plotted with increments of 50 and 100 micro-radians for the 4 μm and 10 μm cases, respectively. It can be observed that the contours of $\frac{\partial w}{\partial x}$ and $\frac{\partial w}{\partial y}$ are symmetric about $x = 0$, but asymmetric about $y = 0$. Accordingly, the contours of $\frac{\partial w}{\partial x}$, $\frac{\partial w}{\partial y}$ and $\frac{\partial w}{\partial r}$ are relatively crowded in the positive y-direction. The noise at the circular clamped boundary and its vicinity in the figures are attributed to measurement errors in r-DGS. The reconstructed 3D surface calculated from HFLI is plotted in figure 12(a). Figure 12(b) shows the

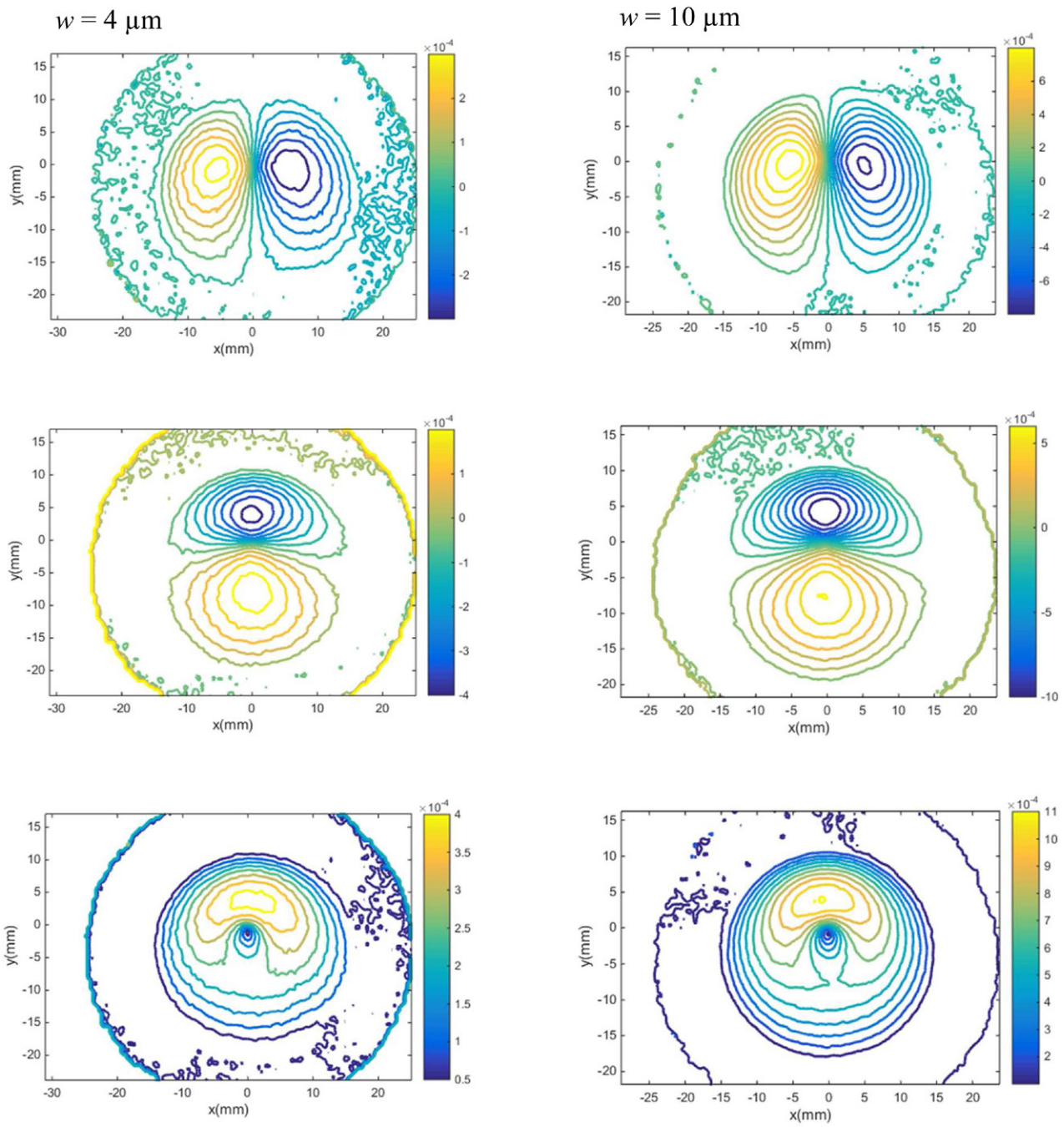

Figure 11. Results from r-DGS for a clamped silicon wafer (30 mm dia., 360 μm thick) subjected to eccentric deflection of 4 μm (left column) and 10 μm (right column). Row 1: contours of $w_{,x}$; Row 2: contours of $w_{,y}$; Row 3: contours of $w_{,r}$. Note: (0, 0) is made to coincide with the loading point. Contour increments = 0.5×10^{-4} rad and 1×10^{-4} rad, respectively.

corresponding contours of out-of-plane displacement (w) at 0.5 μm increments. These plots demonstrate that the shape of the reconstructed surface matches the reality in the experiment. Again, in figures 11 and 12, (0, 0) is made to coincide with the loading point. The peak value of the height of the reconstructed 3D surface is approximately 10.53 μm. Based on the elasticity theory for a circular plate loaded by an eccentric concentrated force [31], the peak value of deflection is 10.16 μm. Further, the location of the theoretical peak value is at ($x = 0, y = -0.8$) or 0.8 mm away from the loading point along the $-y$-direction. Compared with this theoretical value, the reconstruction error is an acceptable 3.6%. The sources of errors are the same as the ones discussed in the previous experiment. Evidently, the reconstructed surface shows asymmetry as expected along with an obvious tilt due to higher stresses and deformation suffered by the epoxy adhesive layer along the boundary close to the loading point relative to the far away edges. That is, the reconstructed shape is tilted towards the positive y-direction, in agreement with the load point eccentricity relative to the center of the wafer.

As in the symmetric loading case, surface reconstruction for $w = 4$ μm case was also carried out and the results are not shown in favor of brevity. The peak value of the height of the reconstructed 3D surface in this case was approximately

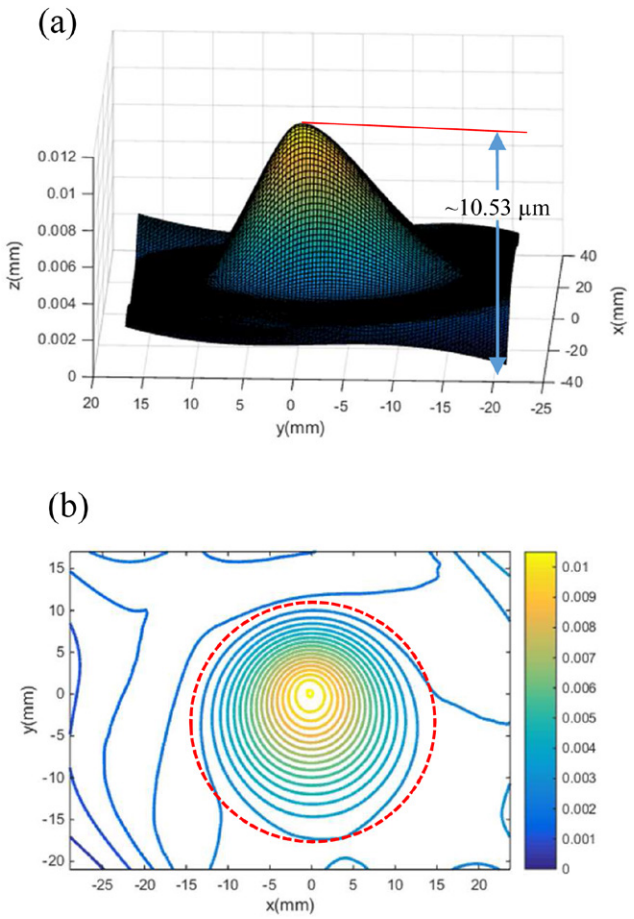

Figure 12. Surface topography calculated via 2D integration using surface slope data and HFLI method: (a) reconstructed 3D surface, (b) out-of-plane displacement (w) contours (0.5 μm increments). Note: (0, 0) is made to coincide with the loading point; red circle is the circular aperture of the steel washer.

5.12 μm with an error of 26% relative to the theoretical value 4.06 μm. Again, due to the uncertainty of the imposed deflection of ± 1 μm, the reconstructed peak value was deemed reasonable.

6. Dynamic mode-I crack propagation in transparent PMMA

The previous two experiments have demonstrated the feasibility of coupling r-DGS methodology with HFLI approach for reconstructing surface profile due to mechanical deformation. Next, the work is extended to transmission-mode DGS (or, t-DGS) to extract stress field data from measured orthogonal stress gradient data to study dynamic crack propagation in brittle polymers such as PMMA. First, the dynamic crack growth in PMMA sheets was studied using t-DGS technique in conjunction with ultrahigh-speed digital photography. The schematic of the experimental setup employed is shown in figure 13. A Hopkinson pressure bar (a 25 mm dia., 1.8 m long 7075-T6 aluminum bar) was used for subjecting a pre-notched (40° V-notch) PMMA specimen to wedge-loading using a gas-gun and a striker bar (a 25 mm dia. and 225 mm long aluminum rod). A Cordin-550 ultrahigh-speed digital camera with 32 independent 1000 × 1000 pixels sensors was used for recording the speckle images during the dynamic fracture event. The specimen was at a distance of approximately 850 mm in front of the camera. A target plate decorated with random black and white speckles was placed behind the specimen at a distance (Δ) 29.3 mm away from the mid-plane of the specimen. The region of interest in this study was in the crack tip neighborhood (52 mm × 52 mm). A pair of heavy dots (figure 14) marked on the target plate were used to relate the dimension on the image to the actual specimen/target dimensions. Prior to loading the specimen, a set of 32 images of the speckles were recorded at 200 000 frames per second through the specimen in its undeformed state. Next, without altering any of the camera settings, the specimen was dynamically loaded by impacting the long-bar with the striker bar (striker velocity ~ 14 m s^{-1}). The impact event triggered recording of a second set of 32 images in the deformed state at the same framing rate. Thus, a total of 32 pairs of images in the deformed and undeformed (reference) states were recorded at 5 μs intervals between successive images. Two representative speckle images in the region of interest, one in the undeformed state and the other in the deformed state are shown in figures 14(a) and (b), respectively. The speckle pattern shown in figure 14(b) corresponds to a time instant 95 μs after crack initiation at the initial notch tip. It can be seen that the speckles are noticeably distorted in the near vicinity of the propagating crack tip (in the deformed image) whereas they seem largely unaffected in the far-field. The corresponding image pairs from each sensor were correlated separately. Further details of the experiment are previously reported by Sundaram and Tippur [29]. During image correlation[5], each image was segmented into 25 × 25 pixels sub-images. An overlap of 20 pixels (i.e. a step size of 5 pixels) was used during analysis. This resulted in 194 × 194 matrix of data points in the region of interest for each of the two orthogonal displacement fields. The corresponding angular deflections of light rays were subsequently determined using the known distance Δ between the specimen and the target planes. Figure 15 shows the angular deflection plots at three select time instants. The crack velocity history for such a crack growth has been previously reported in [29]. Using the angular deflection fields along the x-direction mode-I and mode-II SIFs were evaluated using an over-deterministic least-squares analysis based on the asymptotic expressions for the measured stress gradients (See [29] for details),

$$\phi_x(t) = C_\sigma B \left[\begin{array}{l} -\frac{1}{2} r_l^{-\frac{3}{2}} \left\{ \begin{array}{l} f(V; C_L; C_S) A_I(t) \cos\left(\frac{3\theta_l}{2}\right) \\ +g(V; C_L; C_S) D_I(t) \sin\left(-\frac{3\theta_l}{2}\right) \end{array} \right\} \\ + \sum_{N=2}^{\infty} \left\{ \begin{array}{l} A_N(t) \left(\frac{N}{2} - 1\right) r_l^{\left(\frac{N}{2}-2\right)} \cos\left(\left(\frac{N}{2} - 2\right)\theta_l\right) \\ +D_N(t) \left(\frac{N}{2} - 1\right) r_l^{\left(\frac{N}{2}-2\right)} \sin\left(\left(\frac{N}{2} - 2\right)\theta_l\right) \end{array} \right\} \end{array} \right] \quad (14)$$

[5] The image correlation was carried out in r-DGS also using the image analysis software ARAMIS®.

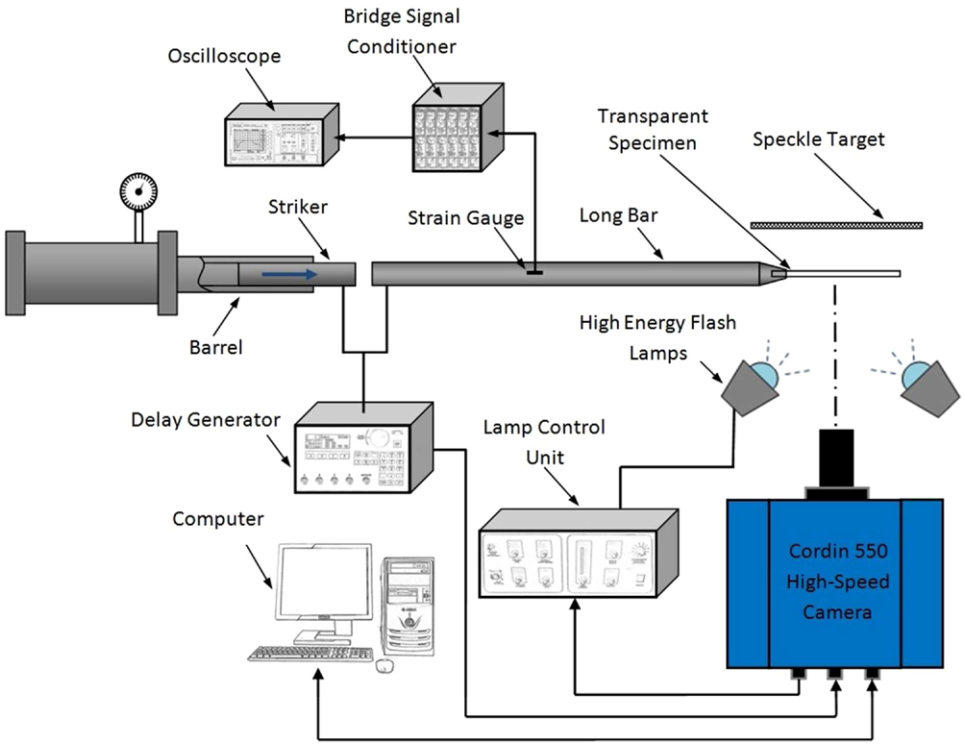

Figure 13. Schematic of the experimental setup used for dynamic fracture study.

where f and g denote functions of instantaneous crack velocity, and (r_l, θ_l) denote the contracted crack tip polar coordinates for a growing crack, C_σ is the elasto-optic constant of the material (-1.08×10^{-10} m^2 N^{-1}), and B is its initial thickness. Further, (r_l, θ_l) can be expressed in the local Cartesian coordinates (x', y') as, $r_l = \{(x')^2 + \alpha_L^2 (y')^2\}^{1/2}$ and $\theta_l = \tan^{-1}\left(\frac{\alpha_L y'}{x'}\right)$. The coefficients of $A_I(t)$ and $D_I(t)$ in the asymptotic series are related to the mode-I and mode-II stress intensity factors (SIF) $K_I(t)$ and $K_{II}(t)$, respectively, as $A_I(t) = K_I(t)\sqrt{2/\pi}$ and $D_I(t) = K_{II}(t)\sqrt{2/\pi}$. The functions f and g are [29],

$$f(V; C_L, C_S) = \left(\frac{1+\nu}{1-\nu}\right)\frac{(1+\alpha_S^2)(1-\alpha_L^2)}{4\alpha_L\alpha_S - (1+\alpha_S^2)^2} \quad \text{and}$$

$$g(V; C_L, C_S) = \left(\frac{1+\nu}{1-\nu}\right)\frac{2\alpha_S(1-\alpha_L^2)}{4\alpha_L\alpha_S - (1+\alpha_S^2)^2} \tag{15}$$

where $\alpha_L = \left[1 - \frac{\rho(1-\nu)}{2\mu}V^2\right]^{\frac{1}{2}}$ and $\alpha_S = \left[1 - \frac{\rho}{\mu}V^2\right]^{\frac{1}{2}}$ for plane stress. Data in the region $(0.25 < r/B < 0.75)$ and $(-135° < \theta < 135°)$ near the crack tip was used for analysis. Figure 16 shows the plot of SIF history evaluated. As this is a mode-I crack growth, K_{II} is expected to be relatively small if not zero. Further, it can be seen that the K_I remains approximately same throughout the window of observation.

Using the SIFs evaluated from the stress gradient fields, the $(\sigma_{xx} + \sigma_{yy})$ fields around the moving crack tip were obtained using the mode-I K-dominant expression for stresses as [30],

$$(\sigma_{xx} + \sigma_{yy}) = \frac{K_I(t)}{\sqrt{2\pi r}} f(\theta = 0, V), \tag{16}$$

where V is the crack velocity,

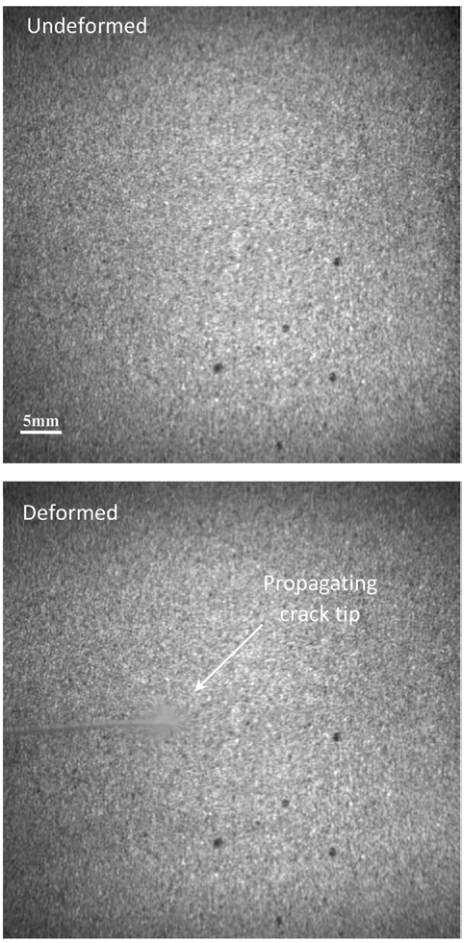

Figure 14. Speckle images in the undeformed (top) and deformed (bottom) states recorded by the high-speed camera though the PMMA specimen.

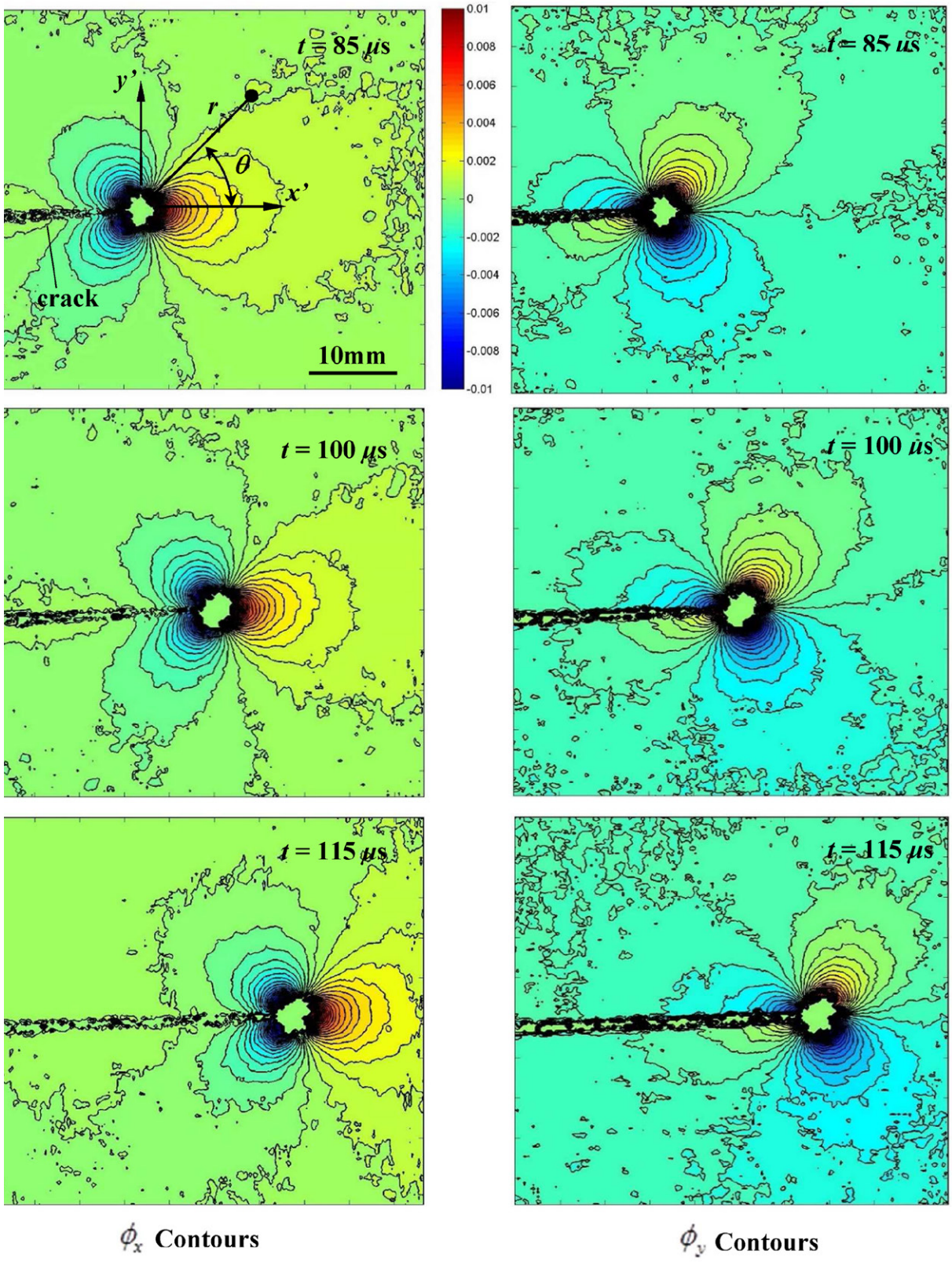

Figure 15. Angular deflection contour plots (contour interval $= 5 \times 10^{-4}$ rad) proportional to stress gradients of $(\sigma_x + \sigma_y)$ in the x- and y-directions.

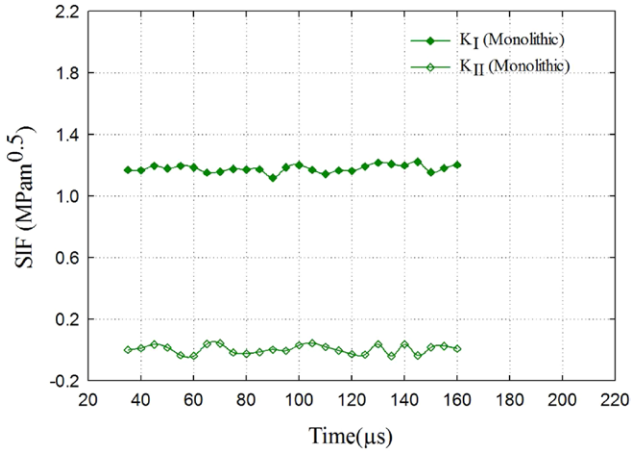

Figure 16. Mode-I and II SIFs for a dynamically growing crack in a monolithic PMMA.

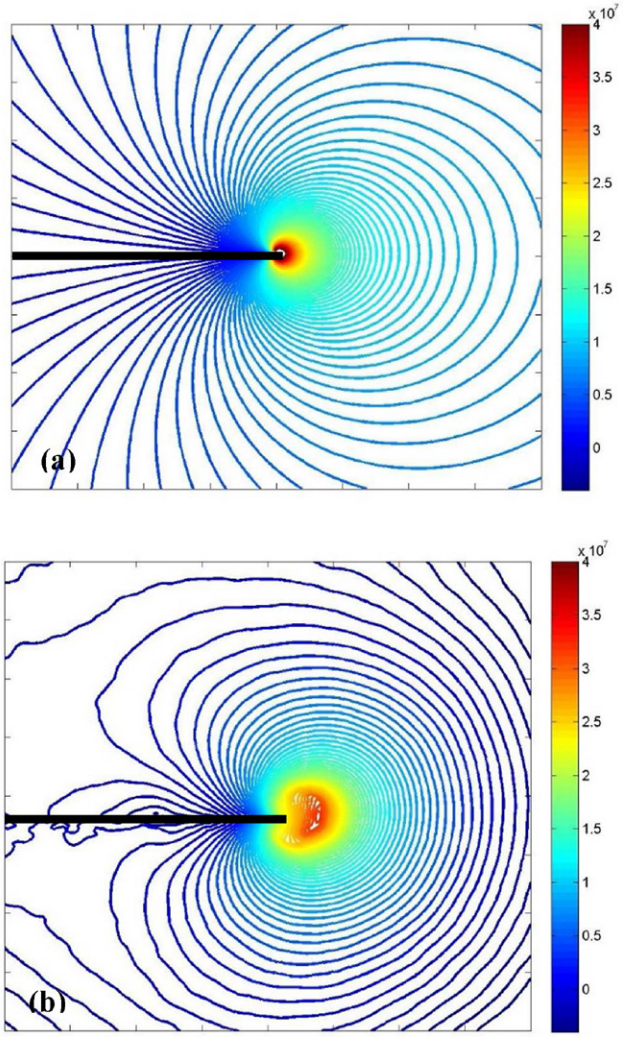

Figure 17. $(\sigma_{xx} + \sigma_{yy})$ fields (contour interval = 0.75 MPa) obtained integration by (a) using K_I and K_{II} measured from the DGS fields along with analytical expression for stress fields and (b) using HFLI method. The black horizontal line represent the growing crack faces.

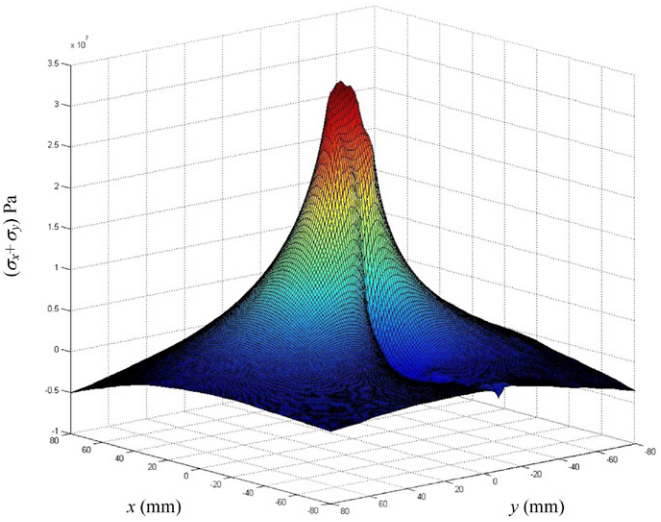

Figure 18. The 3D surface plot of stress around a moving crack tip reconstructed using HFLI.

$$f(\theta; V) = \frac{1}{D}\frac{2\alpha_L^2(1+\alpha_S^2)}{\sqrt{\gamma_L}}\cos\left(\frac{\theta_L}{2}\right),$$

$$D = 4\alpha_S\alpha_L - (1+\alpha_S^2)^2, \alpha_{S;L} = \sqrt{1-\left(\frac{V}{C_{S;L}}\right)^2},$$

$\gamma_{S;L} = \sqrt{1-\left(\frac{V\sin\theta}{C_{S;L}}\right)^2}$, $\tan\theta_{S;L} = \alpha_{S;L}\tan\theta$ and $C_{S;L}$ denote the shear and longitudinal wave speeds of the material. Contour plots of constant $(\sigma_{xx} + \sigma_{yy})$ for a time instant 100 μs after crack initiation are shown in figure 17(a).

The $(\sigma_{xx} + \sigma_{yy})$ fields around the moving crack tip were also obtained by integrating the measured orthogonal stress gradient fields and HFLI method. Figure 17(b) shows the $(\sigma_{xx} + \sigma_{yy})$ fields from HFLI algorithm at a select time instant of 100 μs during dynamic crack growth corresponding to the stress gradient contours shown in figure 17(a). It can be seen that both the stress fields have qualitative similarities near the crack tip vicinity. However, it should be emphasized that the reconstructed stresses, unlike the theoretical counterpart, encompass all the far-field effects (or, the higher order terms). In light of this, the contours do deviate both qualitatively and quantitatively from the ones shown in figure 17(a) based on *K*-dominant (one-term description) in equation (16). The 3D surface plot of reconstructed stress around the crack tip is shown in figure 18 that indicates severe stress amplification in the immediate crack tip vicinity.

To compare the $(\sigma_{xx} + \sigma_{yy})$ fields obtained from these two methods more effectively, $(\sigma_{xx} + \sigma_{yy})$ values were evaluated at select directions namely $(r, \theta = 0°)$ and $(r, \theta = 45°)$ relative to the crack tip ($\theta = 0°$ denotes crack growth direction) are plotted in figure 19. We can see a good agreement between the two plots in the region $(0.25 < r/B < 0.75)$ where the data was selected for performing the least-squares analysis. For $r/B > 0.75$ the *K*-dominance is lost and for $r/B < 0.25$ there is

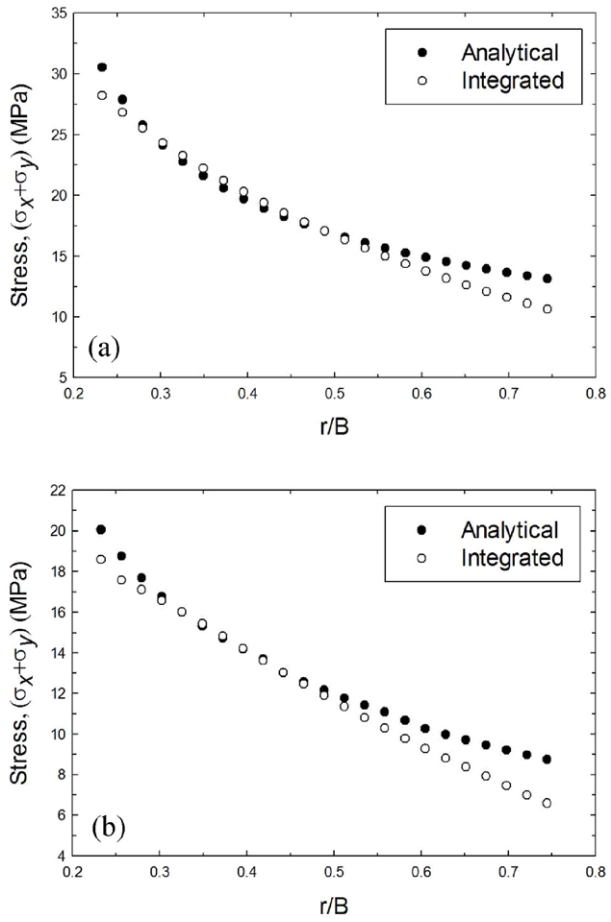

Figure 19. The plot of stress evaluated from integration and by using K-dominant equations from the extracted SIFs for a direction of (a) 0°, and (b) 45° from the crack growth direction.

significant stress triaxiality whereas contours based on equation (16) are based on 2D (plane stress) assumptions.

7. Conclusions

In this work, the feasibility of surface profile evaluation and stress field mapping from r-DGS and t-DGS methods are demonstrated. This is accomplished by coupling DGS output with a HFLI scheme implemented in the Southwell configuration. DGS being a DIC-based method capable of providing two orthogonal gradients simultaneously, it naturally lends itself to the implementation of algorithms in the Southwell configuration.

First, the surface profile measurements are demonstrated successfully using a 'clamped' reflective Si wafer subjected to out-of-plane concentrated load applied centrally and eccentrically in two separate sets of experiments. The imposed deflection has been recovered using the HFLI scheme with good accuracy relative to the accuracy of the micrometer used. For 10 ± 1 μm imposed deflection cases, the recovered values show approximately 5% deviation from the expected value. The reconstruction has also revealed non-zero out-of-plane deflections in the 'clamped' regions of the plate due to the compliance of the epoxy adhesive layer. The phenomenon is pronounced in the eccentric loading case with the glued edge closer to the loading point show higher deflections relative to the far-away edge. The analysis of data with different data intervals show that the method is quite robust and the peak value variations are relatively negligible among the three cases considered.

Further, reconstruction of $(\sigma_{xx} + \sigma_{yy})$ stress fields from stress gradients is demonstrated for the case of a dynamically growing crack in a transparent polymer (PMMA) sheet. For a time instant of 100 μs after crack initiation, the stress gradient fields used in conjunction with HFLI algorithm resulted in obtaining stress fields with qualitative similarities to the theoretical (or, the so-called *K*-dominant) counterparts. The comparison was limited because the crack tip SIF were evaluated by analyzing measured gradients close to the crack tip in conjunction with the asymptotic series expansion based on 2D assumptions. Accordingly, only the first coefficient (K_I) of the expansion was used to recreate the theoretical stress fields. The reconstructed/experimental stresses and the theoretical values agree quite well in the crack tip vicinity although they deviate from each other due to the higher order effects far away from the crack tip and due to triaxial effects very close to the crack tip.

Acknowledgments

The corresponding author acknowledges partial support of this research through Department of Defense grants W31P4Q-14-C-0049 and ARMY-W911NF-16-1-0093.

References

[1] Malacara-Doblado D and Ghozeil I 2007 Hartmann, Hartmann–Shack, and other screen tests *Optical Shop Testing* 3rd edn, ed D Malacara (Hoboken, NJ: Wiley)
[2] Strojnik M, Paez G and Mantravadi M 2007 Lateral shear interferometers *Optical Shop Testing* 3rd edn, ed D Malacara (Hoboken, NJ: Wiley)
[3] Ragazzoni R 1996 Pupil plane wavefront sensing with an oscillating prism *J. Mod. Opt.* **43** 289–93
[4] Ettl S, Kaminski J, Knauer M and Häusler G 2008 Shape reconstruction from gradient data *Appl. Opt.* **47** 2091–7
[5] Assa A, Betser A A and Politch J 1997 Recording slope and curvature contours of flexed plates using gratings shearing interferometer *Appl. Opt.* **16** 2504–13
[6] Kao T Y and Chiang F P 1982 Family of grating techniques of slope and curvature measurements for static and dynamic flexure of plates *Opt. Eng.* **21** 721–42
[7] Tippur H V 2004 Simultaneous and real-time measurement of slpoe and curvature fringes in thin structures using shearing interferometry *Opt. Eng.* **43** 3014–20
[8] Tippur H V, Krishnaswamy S and Rosakis A J 1991 Optical mapping of crack tip deformations using the methods of transmission and reflection coherent gradient sensing-a study of crack tip *K*-Dominance *Int. J. Fract.* **52** 91–117
[9] Ritter R 1982 Reflection moire methods for plate bending studies *Opt. Eng.* **21** 663–71
[10] Sutton M A, Orteu J J and Schreier H 2009 *Image Correlation for Shape, Motion and Deformation Measurements: basic concepts, theory and applications* (New York: Springer)
[11] Kirugulige M S, Tippur H V and Denney T S 2007 Measurement of transient deformations using digital image correlation method and high-speed photography: application to dynamic fracture *Appl. Opt.* **46** 5083–96

[12] Chu T C, Ranson W F, Sutton M A and Peters W H 1985 Application of digital image correlation techniques to experimental mechanics *Exp. Mech.* **25** 232–44
[13] Chen D J, Chiang F P, Tan Y S and Don H S 1993 Digital speckle-displacement measurement using a complex spectrum method *Appl. Opt.* **32** 1839–49
[14] Periasamy C and Tippur H V 2012 Full-field digital gradient sensing method for evaluating stress gradients in transparent solids *Appl. Opt.* **51** 2088–97
[15] Periasamy C and Tippur H V 2013 Measurement of orthogonal stress gradients due to impact load on a transparent sheet using digital gradient sensing method *Exp. Mech.* **53** 97–111
[16] Periasamy C and Tippur H V 2013 A full-field reflection-mode digital gradient sensing method for measuring orthogonal slopes and curvatures of thin structures *Meas. Sci. Technol.* **24** 025202
[17] Coleman N E and Jain R 1982 Obtaining 3-dimensional shape of textured and specular surfaces using four-source photometry *Comput. Vis. Graph. Image Process.* **18** 309–28
[18] Healey G and Jain R 1984 Depth recovery from surface normals *Int. Conf. on Pattern Recognition* vol 2, pp 894–6
[19] Wu Z and Li L 1988 A line-integration based method for depth recovery from surface normals *Comput. Vis. Graph. Image Process.* **43** 53–66
[20] Frankot R T and Chellappa R 1988 A method for enforcing integrability in shape from shading algorithms *IEEE Trans. Pattern Anal. Mach. Intell.* **10** 439–51
[21] Hudgin R H 1977 Wave-front reconstruction for compensated imaging *J. Opt. Soc. Am.* **67** 375–8
[22] Southwell W H 1980 Wave-front estimation from wave-front slope measurements *J. Opt. Soc. Am.* **70** 998–1006
[23] Huang L and Asundi A 2012 Improvement of least-squares integration method with iterative compensations in fringe reflectometry *Appl. Opt.* **51** 7459–65
[24] Li G, Li Y, Liu K, Ma X and Wang H 2013 Improving wave front reconstruction accuracy by using integration equations with higher-order truncation errors in the Southwell geometry *J. Opt. Soc. Am.* A **2013** 1448–59
[25] Klette R and Schlüns K 1996 Height data from gradient fields *Proc. SPIE* **2908** 204
[26] Huang L, Idir M, Zuo C, Kaznatcheev K, Zhou L and Asundi A 2015 Comparison of two-dimensional integration methods for shape reconstruction from gradient data *Opt. Laser Eng.* **64** 1–11
[27] Jain A S and Tippur H V 2016 Extension of reflection-mode digital gradient sensing method for visualizing and quantifying transient deformations and damage in solids *Opt. Laser Eng.* **77** 162–74
[28] Malacara D 1992 *Optical Shop Testing* 2nd edn (New York: Wiley)
[29] Sundaram B M and Tippur H V 2016 Dynamic crack growth normal to an interface in bi-layered materials: an experimental study using digital gradient sensing technique *Exp. Mech.* **56** 37–57
[30] Paris P C and Sih G C 1965 *Stress Analysis of Cracks, Fracture Toughness Testing and its Applications* (ASTM Special Technical Publication) No. 381 pp 30–81
[31] Ventsel E and Krauthammer T 2001 *Thin Plates and Shells: Theory, Analysis and Applications* (New York: CRC Press)